Multi-scale morphologic investigation of craters in the Chang'e-4 landing area

Mengna Jia [a,b], Kaichang Di [a,c,f], Zongyu Yue [a,f], Bin Liu [a,*,1], Wenhui Wan [a], Shengli Niu [c], Jianzhong Liu [d,f], Weiming Cheng [e,f], Yangting Lin [g]

[a] *State Key Laboratory of Remote Sensing Science, Aerospace Information Research Institute, Chinese Academy of Sciences, Beijing 100101, China*
[b] *China Academy of Space Technology (Xi'an), Xi'an 710100, China*
[c] *State Key Laboratory of Lunar and Planetary Sciences, Macau University of Science and Technology, Macau 999078, China*
[d] *Institute of Geochemistry Chinese Academy of Sciences, Guiyang 550002, China*
[e] *Institute of Geographic Sciences and Natural Resources Research, Chinese Academy of Sciences, Beijing 100101, China*
[f] *CAS Center for Excellence in Comparative Planetology, Hefei 230026, China*
[g] *Key Laboratory of Earth and Planetary Physics, Institute of Geology and Geophysics, Chinese Academy of Sciences, Beijing 100029, China*

ARTICLE INFO

ABSTRACT

China's Chang'e-4 (CE-4) rover landed in Von Kármán crater on January 3, 2019, and has acquired a large amount of data of the landing site. Craters are an important landform in lunar surface and the analysis of craters at the landing site with high-resolution images is of great significance for both scientific study and engineering safety. In this study, multi-sources data, including Lunar Reconnaissance Orbiter Camera Narrow Angle Camera (NAC) images, NAC digital elevation model (DEM), Chang'e-2 (CE-2) digital orthophoto map (DOM), SLDEM2015 and stereo images from panoramic cameras onboard the CE-4 rover, are involved to reveal the crater morphologic features at the landing site. The diameter, depth, spatial density and depth/diameter ratio (*d/D*) of the mapped craters have been investigated. Randomness analysis and the size-frequency distributions of craters in two scales are conducted to thoroughly elaborate the crater distribution in the landing area. The multi-scale crater investigation establishes a foundation for subsequent in-depth studies, e.g., crater evolution and degradation of lunar farside and CE-4 landing area dating.

1. Introduction

Chang'e-4 (CE-4) mission is China's second lunar soft landing mission and it was initially designed as the back-up of Chang'e-3 (CE-3) mission, both of which constitute the second phase of China Lunar Exploration Project (CLEP, 2018; Jia et al., 2018). CE-4 mission includes a communication relay satellite, a lander, and a rover (Yutu-2). The relay satellite (Magpie Bridge), which was launched on May 5, 2018, provides Earth-Moon relay communications between the CE-4 lunar probe and the control center in the Earth (Gao et al., 2019; Qin et al., 2019). The CE-4 probe was launched on December 8, 2018 and successfully landed in the Von Kármán crater at (177.588°E, 45.457°S) on January 3, 2019 (Di et al., 2019a).

The Von Kármán crater was formed in pre-Nectarian period and it is inside the oldest, deepest, and largest lunar basin, i.e., the South-Pole

Aiken (SPA) basin. The SPA basin was thought to have exposed the lunar lower crust and probably upper mantle material according to the spectral analysis of remote sensing observations and numerical impact cratering simulations (e.g., Head et al., 1993; Lucey et al., 1998; Ohtake et al., 2014; Melosh et al., 2017). The in-situ investigation by CE-4 provides a unique opportunity for in-depth research. CE-4 mission has returned a large amount of data with the onboard payloads including a landing camera, a terrain camera, a pair of panoramic cameras, a visible and near-infrared imaging spectrometer, and ground penetrating radar (Wu et al., 2019). Much information on the lunar farside, such as the composition of the deep material (Gou et al., 2019; Li et al., 2019), local mineral abundances (Hu et al., 2019), and topographic evolution (Di et al., 2019b), have been obtained and more findings are expected with the ongoing interpretation of the returned data.

As one of the most important landforms in lunar surface, craters are

---

* Corresponding author.
  E-mail address: liubin@radi.ac.cn (B. Liu).
[1] Address: P. O. Box 9718, Datun Road, Chaoyang District, Beijing, 100,101, China

significant in understanding the geologic history (Wilhelms et al., 1987), subsurface composition and structure (Soderblom et al., 1974; Bland et al., 2016), surface gardening process (Melosh, 1989), etc. Therefore, much work has been carried out in lunar crater study, especially creating catalogues of global or regional craters and making related analyses. However, the existing lunar global crater catalogues are generally established using low-resolution images. For example, the most recently created lunar global crater database is mainly based on Lunar Reconnaissance Orbiter Camera (LROC) Wide Angle Camera (WAC) mosaic at 100 m/pixel and the minimum diameter of the craters is ~1.0 km (Robbins, 2019). On the other hand, the near global covering of LROC Narrow Angle Camera (NAC) images at the resolution of ~0.5–2.0 m/pixel and the returned panoramic camera (PanCam) images by Yutu-2 rover have offered the opportunity for creating a much finer regional crater catalogue. It is significant for understanding of impact physics at this scale, estimating the gardening process in lunar shallow surface, interpreting the returned data especially for the ground penetrating radar, and even for evaluating the engineer safety in future rover traveling.

In this research, a 0.9 m-resolution DOM mosaic is produced from the LROC NAC images, based on which two different-scaled crater catalogues are established. Besides, smaller scaled craters are also digitalized from stereo images obtained by the PanCam mounted on the CE-4 rover. According to these catalogues, the crater-related morphological features in the landing area, including multi-scale spatial density, depth/diameter ratio (*d/D*) and size-frequency distribution (SFD), etc., are investigated in detail.

2. Data and method

2.1. Data

The datasets used in this study include images from LROC NAC (Robinson et al., 2010), Chang'e-2 (CE-2) CCD camera (CLEP, 2018), and Yutu-2 rover PanCam. Topographic data from SLDEM2015 (Barker et al., 2016) and LROC NAC image generated DEM (Henriksen et al., 2017) are used for depth measurements. The LROC NAC images and DEM products, and SLDEM2015 can be downloaded from the Planetary Data System (PDS) Geosciences Node (https://ode.rsl.wustl.edu/moon/), while the CE-2 CCD digital orthophoto map (DOM) can be obtained from the website of Data Publishing and Information Service System (DPISS) of CLEP (http://moon.bao.ac.cn/).

The LROC NAC images are generally at the resolutions ~0.5–2.0 m/pixel, which are the highest resolution lunar orbital images available at present (Robinson et al., 2010). LROC NAC DEMs are generated by two NAC images covering the same area on the ground while taken from different view angles (Henriksen et al., 2017). The NAC DEM used in this study has a ground sample distance of 5.0 m and was created from stereo images of M1303619844 and M1303640934 (Robinson, 2019).

The two-line push-broom time delay and integration CCD camera is one of the important payloads of CE-2 mission. It is composed of a forward-looking and a backward-looking line camera to obtain orbital stereo images. The CE-2 stereo cameras acquired stereo images of global coverage at a resolution of 7 m/pixel in a 100 km × 100 km polar circular orbit (Zhao et al., 2011). The global 7 m DOM product of CE-2 has been produced and released on DPISS website (http://moon.bao.ac.cn/; CLEP, 2018).

The SLDEM2015 was generated by a combination of LRO Lunar Orbiter Laser Altimeter and DEMs from stereo images obtained by Kaguya Terrain Camera. SLDEM2015 covers latitudes within ±60° and has an effective resolution of approximately 60 m/pixel at the equator and a typical vertical accuracy of 3 m–4 m (Barker et al., 2016).

The selected landing area for CE-4 is within 176.4°E-178.8°E, 45°S-46°S (Fig. 1a). To generate the high-resolution DOM in the CE-4 landing area, 100 LROC NAC Experimental Data Record (EDR) level images with similar illumination condition and good imaging quality were selected.

The radiometrical and geometric corrections are subsequently made to these EDR level NAC images with the software of Integrated System for Imagers and Spectrometers (ISIS) (Anderson et al., 2014). Then, a program is developed to process the geometric inconsistencies between NAC images (Liu et al., 2019). Unfortunately, there are some gaps between some LROC NAC images, and then one CE-2 DOM image (CE2_GRAS_DOM_07m_K136_45S175E_A) is used for these areas. The final DOM mosaic of the landing area is shown in Fig. 1b in a Lambert conformal conic projection, which has a ground sample distance of ~0.9 m and an image size of 57,483 columns × 34,084 rows.

The PanCam on the CE-4 rover comprises two identical cameras with 19.7° × 14.5° field of view, which can obtain stereo image pairs around the rover with a baseline of 270 mm (Jia et al., 2018). The PanCam has the ability of 360° imaging with the assistance of the rotary stage and the acquired images have the size of 2352 pixels × 1728 pixels. The PanCam images used in this study were obtained during the first lunar day of the mission (Di et al., 2019b) and 58 stereo pairs were adopted for crater measurement. The data can also be downloaded from the DPISS website (http://moon.bao.ac.cn/). It is worth noting that very small craters surrounding the landing site are affected by rocket engine plume during soft landing. The affected region (Gou et al., 2020) is mainly distributed on the western direction of the lander and PanCam images in this study is obtained at the northwest of the lander with a straight-line distance of ~16 m. Therefore, the rocket engine plume effect is very limited in the research area of this study.

2.2. Crater mapping and analysis in CE-4 landing area

The craters in the CE-4 landing area are mapped in three scales based on the produced DOM, the DEMs (entire landing area or local area surrounding the landing site) or the PanCam stereo images. Within 1° in latitude and 2.4° in longitude (30 km × 51 km) LROC NAC mosaic in the landing area (Fig. 1b), craters with the minimum diameter of ~100 m are mapped, and their depth are measured with SLDEM2015. For a small area of 3.2 km × 3.0 km surrounding the landing site (red rectangular in Fig. 1a), where a very high-resolution DEM of ~5 m/pixel is available, craters larger than several meters are mapped and measured. It can be inferred from previous researches (Fig. 2b of Huang et al., 2018 and Fig. 5c of Qiao et al., 2019) that the local slope for the CE-4 landing area is very small and the slope effect could be ignored in the following investigation.

When mapping the craters with the NAC mosaic, crater rims are first manually extracted with an ArcGIS add-in tool of "CraterTools", which is independent of the projection and has been widely used in planetary crater mapping (Kneissl et al., 2011; Povilaitis et al., 2018). In addition, to digitalize crater rims more precisely, a local tangent plane projection is adopted and the projection center is set at the center of the research area. A strategy of fitting the crater with three evenly distributed points on their rims is always used. When applicable, the mapped crater rims are further optimized with another ArcGIS add-in tool developed by Liu et al. (2018) with the assistant of SLDEM2015 and NAC DEM for both the larger and smaller classes of craters, respectively. The rim-to-floor depths of these craters are also automatically calculated with the ArcGIS add-in tool by Liu et al. (2018).

Much smaller craters, in sub-meter or meter scale in diameter, are mapped in the PanCam images from CE-4 rover. A program is developed for crater mapping and measurements in the PanCam stereo images. Fig. 2 shows a pair of stereo images from the PanCam. Two rim endpoints of one diameter line of the crater are manually identified in the left image, and the corresponding points in the right image are automatically matched. Consequently, the 3-D ground coordinates of these endpoints are calculated by triangulation with the assistance of the image interior and exterior orientation parameters. As a result, the crater diameter is derived as the distance between the two rim points.

The rim-to-floor depth of a crater from PanCam stereo images is calculated as the distance between crater floor and the fitted rim plane.
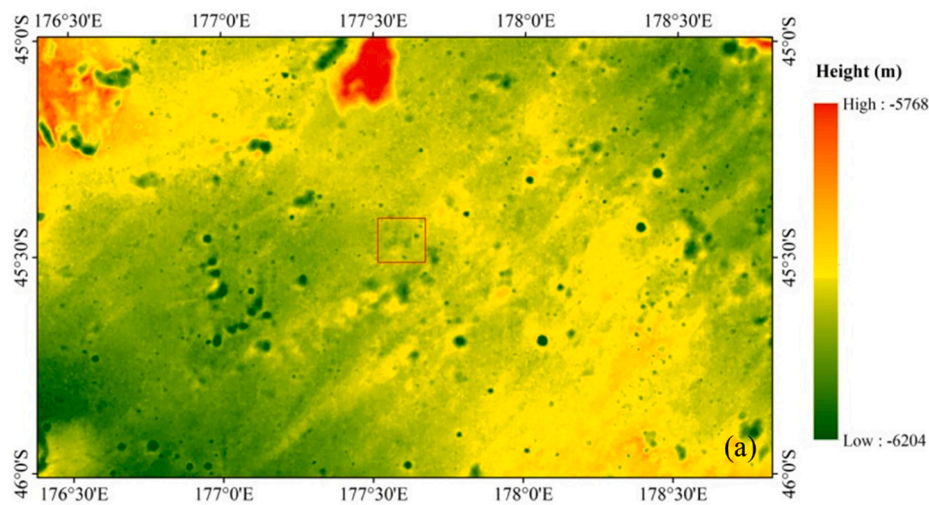
Fig. 1. (a) Crater mapping areas in the research. Craters larger than 100 m in diameter are mapped in the above whole area, and their depths are measured with SLDEM2015. The craters larger than several meters in diameter are mapped within the red rectangle, and the depths are measured with an available high resolution DEM from LROC NAC stereo images. The basemap is SLDEM2015 (Barker et al., 2016). (b) The mapped craters larger than 100 m in the CE-4 landing area overlaid on the LROC NAC DOM mosaic. (c) The distribution of the mapped craters in the 3.2 km × 3.0 km area surrounding the CE-4 landing site. The white arrow in (c) points to a relatively fresh crater, whose detailed information can be found in Table 1 (Crater ID: C1). The craters larger than the completeness diameters (127 m and 9 m for (b) and (c) respectively) are plotted in red while the smaller ones are in yellow. The CE-4 landing site is marked as the white crosses in (b) and (c). (For interpretation of the references to colour in this figure legend, the reader is referred to the web version of this article.)
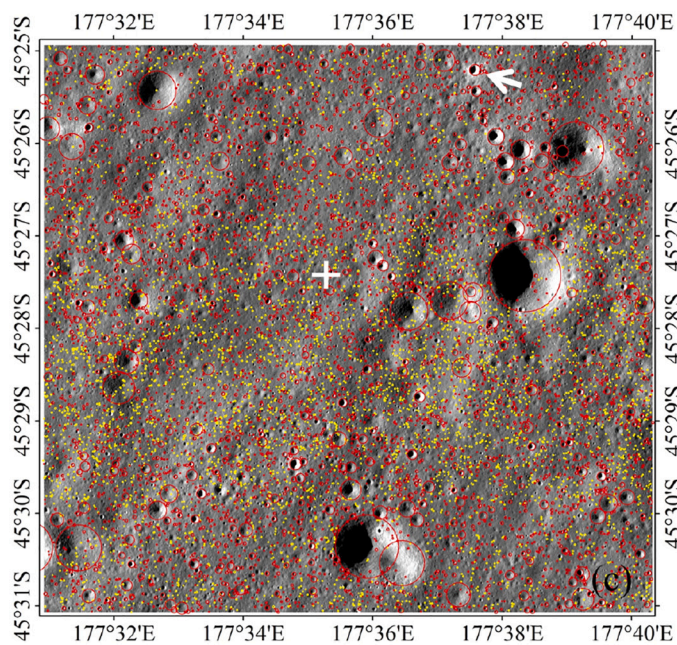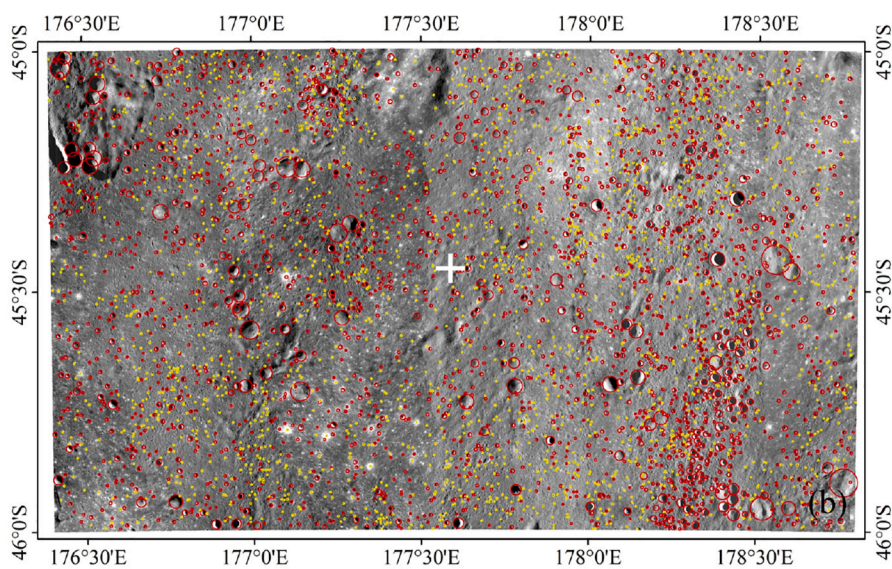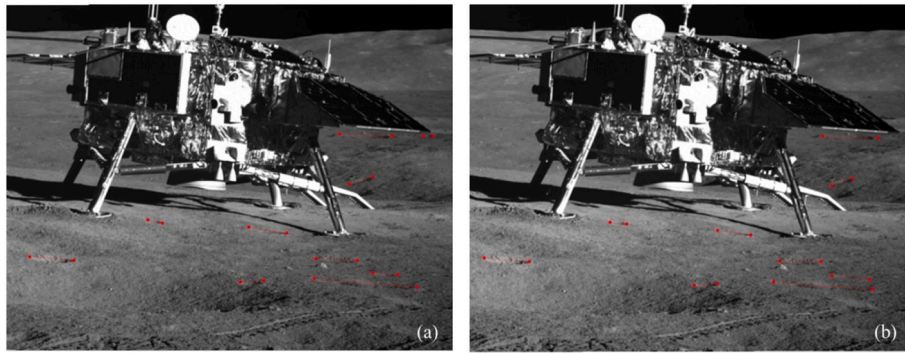
Fig. 2. Crater measurement from a pair of PanCam images. The crater rim points at the ends of one diameter line are manually identified in the left image (a), and the corresponding homologous points are automatically obtained in the right image (b). The diameter of the crater is finally derived as the distance of the two end points.

To be specific, a series points distributed evenly on the crater rim (red crosses in Fig. 3) and a profile crossing the crater floor (green crosses in Fig. 3) are identified, respectively. Their ground coordinates are calculated by photogrammetric method. A plane is fitted with the rim points and the distance from each green point on the profile to the fitted plane is calculated. A quadratic polynomial is adopted to fit the resultant distances, and the final crater depth is searched as the distance at the fitted vertex. By this way, the influence of topographic undulation on depth measurement can be alleviated.

To further reveal the crater population, the randomness analysis function in the CraterStats2 tool (Michael et al., 2012) is used, which can quantitatively describe the crater clustering condition at different size ranges relative to a series of randomly distributed populations (Michael et al., 2012). In the process, craters are separated into several groups according to diameters in a $\sqrt{2}$-spaced interval. A Monte Carlo simulation is then used to give the random distribution of samples in each group and meanwhile the crater size and the counting area are all considered. The measured distance between craters is taken as the parameter to evaluate the randomness by comparing the real measurement and the simulated result. If the former is far below the expected value, it proves that the population is non-random and more clustered, while if the distance measurement lies within the bulk of the histogram, it indicates that the test does not reject randomness and craters are more likely in random distribution. In this study, the selected parameter is "mean 2nd-closest neighbor distance (M2CND)" and the iteration times of the Monte Carlo simulation is set to be 10,000.
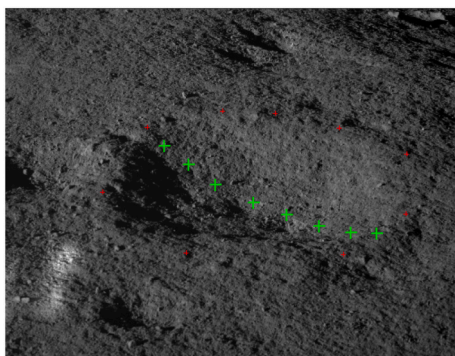
3. Catalogue of craters in CE-4 landing area

Fig. 1b shows the mapped craters in the landing area with DOM mosaic from LROC NAC and the corresponding incremental SFD is shown in Fig. 4 with blue stars. The mapping result shows that the diameter (*D*) corresponding to the peak number is ~100 m, and the completeness diameter is determined as 127 m with the method proposed by Robbins et al. (2018). There are totally 4333 craters mapped in the landing area, within which 3760 and 2298 craters are larger than 100 m (yellow circle in Fig. 1b) and 127 m (red circle in Fig. 1b), respectively. Besides, 97 and 13 craters have diameters larger than 500 m and 1 km, respectively.

In the 3.2 km × 3.0 km area surrounding the landing site, we tried to digitalize all measureable craters and finally 11,787 craters from several meters to more than hundred meters in diameter are mapped. The completeness diameter is found to be 9 m and all craters are depicted in Fig. 1c with the red circles indicating the 5108 craters larger than 9 m and yellow for the residual craters. There are 27 craters larger than 100 m with the largest being 393 m, while the smallest crater measured in the area is ~3.6 m subjected to limitation of the image resolution. The incremental SFD of craters in this scale is shown in Fig. 4 with red circles.

For mapping craters from PanCam images, only those craters within the distance to the rover less than 60 m are mapped in this study. This is because the measurement precision with PanCam images will decrease greatly in the far distance. Totally, 738 craters surrounding the rover are
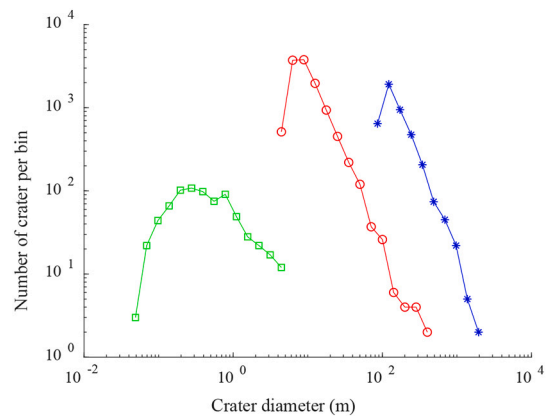

Fig. 3. Points used to determine the crater depth from PanCam stereo images. The crater rim plane is fitted by points labeled with red small crosses, and some green crosses passing through the crater center as much as possible are also identified. The crater depth is defined as the distance from the vertex of the fitted profile to the fitted crater rim plain. See text for details. (For interpretation of the references to colour in this figure legend, the reader is referred to the web version of this article.)

Fig. 4. The incremental size-frequency distribution of craters shown in a log-log plot. The diameter interval is $\sqrt{2}D$ m and the crater diameter refers to the middle value of each bin. The blue "*"s represent the results of craters mapped from the 2.4° × 1° landing area. Craters from the 3.2 km × 3.0 km area surrounding the landing site are indicated by red circles. The green squares show craters from PanCam images. (For interpretation of the references to colour in this figure legend, the reader is referred to the web version of this article.)

mapped and measured from the PanCam stereo images (Fig. 5), and most of the mapped craters (95%) are within the distance of 30 m to the rover. There are several large craters with the diameters ~25 m surrounding the lander, and because they can also be observed from the NAC mosaic, they are not included in the PanCam image crater analysis.

The largest crater measured from PanCam images has a diameter of 4.66 m (labeled by No.1 in Fig. 5b) and it is ~27 m far from the rover. Totally, there are 21 mapped craters larger than 3 m, ~85% of the craters are smaller than 1 m, and ~ 7% of them are in centimeter level. The mean diameter of the whole catalogue is ~0.62 m. The size-frequency distribution of the mapped craters is shown in Fig. 4 with green square. It seems that the decrease of frequency as diameter increases for craters larger than 0.8 m tends to be stable. However, we do not attempt to get a completeness diameter for craters from PanCam images, because the optical sight line of PanCam is approximately parallel to the lunar surface, resulting in the heavily sheltering of craters in topographic undulated area. Similarly, we do not analyze the crater spatial density from PanCam images either.

The depth (*d*) of the craters measured from the NAC DOM mosaic is further automatically calculated by the ArcGIS add-in tool developed by Liu et al. (2018) with the assistant of SLDEM2015 and the NAC DEM. Subject to the ground sample distance and height precision of SLDEM2015, the depth of 110 craters larger than 480 m in diameter are measured. There are four craters deeper than 100 m, which are all distributed in the eastern part of the landing area, and the deepest one is 169 m with the diameter of 956 m. In addition, approximately 33% of crater depths are less than 25 m. The relationship between the diameter and the depth of these 110 craters are displayed in Fig. 6a with red triangles.

The height precision of the released LROC NAC DEM adopted in this research is ~1.1 m (Robinson, 2019; http://lroc.sese.asu.edu/). Thus, the depths of 28 craters deeper than 5 m and with the size range of ~60 m–393 m are obtained from the NAC DEM and the results also demonstrated in Fig. 6 (blue diamonds). The maximum depth is 42 m corresponding to the crater with the diameter of ~393 m. Twenty-three craters, or 82% of the total measured craters, have the depth within 5 m–14 m, and their diameters ranging from 60 m to 320 m.

Subjected to the variation of the resolution and illumination conditions of PanCam images, the depths of only 20 craters (labeled with green in Fig. 5) are measured and ~ 80% of them are less than 10 m to the rover. The depth of the 20 craters is shown in Fig. 6a with green crosses, and all of them are shallower than 0.6 m. Among the 20 craters, the diameters of the largest two are ~4.3 m, both of which are more than 30 m far from the rover, and they also have the largest depths (0.36 m and 0.26 m).

The relationship between diameter and depth of all depth-attainable craters in this research is fitted with a power law as done in previous studies (e.g., Wood and Anderson, 1978; Daubar et al., 2014; Sun et al., 2018) and the result is $d = 0.0726D^{0.9493}$. The exponent is close to 1.0, indicating the depth and the diameter of the craters are almost linear. However, a linear fitting of the diameter and depth get unsatisfactory results in this study ($R^2 = 0.37$), which greatly diverge from smaller craters.

Fig. 6b shows the variation of the *d/D* against the diameter of the mapped craters in CE-4 landing area. The crater *d/D* in the research area has a wide distribution especially for large craters measured from the SLDEM2015, ranging from 0.02 to 0.18 with the mean value of 0.06. For craters with the depth measured from SLDEM2015, the top several craters in Fig. 6b with *d/D* less than 0.04 have relatively shallower depth and are possibly secondary craters or eroded craters. There are 18 craters with *d/D* larger than 0.1 and the largest one corresponds to the crater of 956 m in diameter, most of which are fresh primary craters by visual interpretation. From Fig. 7, the bin with *d/D* centered in 0.04 contains the largest crater numbers for craters with depth measured from SLDEM2015, closely followed by the bin centered in 0.02, and craters with *d/D* smaller than 0.06 accounting for 61% of the group.

The *d/D* of craters measured from NAC DEM is all less than ~0.14, with the mean value of ~0.07. Six craters have *d/D* larger than 0.1, spreading in all size ranges (60 m to 393 m). Compared with craters measured from SLDEM, the crater number distribution of *d/D* for this group is more uniform especially between 0.01 and 0.09 (Fig. 7).

As demonstrated in Fig. 6b, the *d/D* of craters measured from the PanCam images ranges from 0.04 to 0.12 with the mean value of 0.07, only two of which are larger than 0.1. The largest *d/D* corresponds to a crater diameter of 0.5 m, and this crater is on the east of the rover with a distance of about 4.1 m (labeled by No.2 in Fig. 5a). The *d/D* for this group of craters mainly concentrates between 0.05 and 0.09, up to 70% of whole group (Fig. 7). The detailed comparison of the *d/D* can be found in Section 4.4.

The spatial density of craters larger than 127 m in the landing area is analyzed in a 500 m × 500 m grid with a search radius of 1 km (Fig. 8a). The high-density areas are mainly between 178.0°E and 178.5°E and several other high-density clusters scattered elsewhere. By comparing with Fig. 1b, all these high-density areas correspond to secondary chains or clusters, indicating that secondary craters are very widespread in the landing area. After removing possible secondary craters (Fig. 8b), the spatial density of craters tends to be more evenly distributed, although the eastern part still has higher spatial density than that in the west.
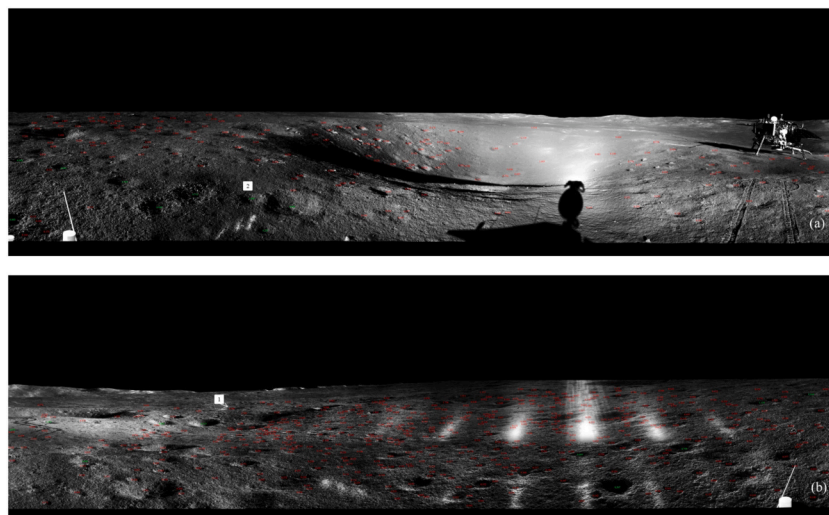

Fig. 5. The mapped craters from the PanCam images with diameters annotated. The sub-figure (a) and (b) together make up the full 360° PanCam mosaic.
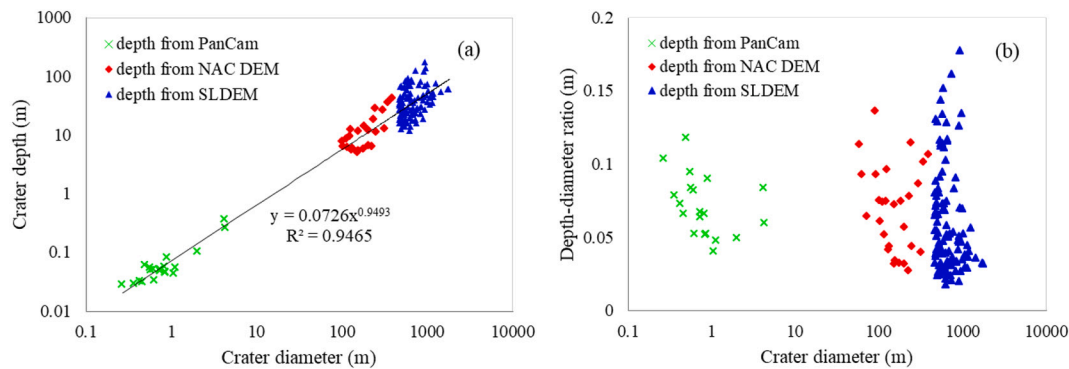
Fig. 6. The relationship between the diameter and (a) depth, (b) depth/diameter ratio for craters in the landing area. The samples with different colors and shapes indicate craters measured from PanCam, NAC DEM and SLDEM2015, respectively.
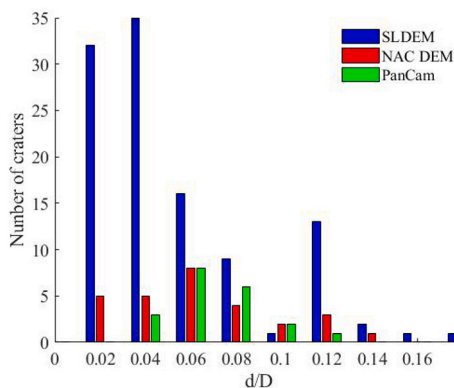

Fig. 7. Histogram of d/D of craters with depth measured from SLDEM2015 (blue), NAC DEM (red) and PanCam image (green), the bin interval is set to be 0.02. (For interpretation of the references to colour in this figure legend, the reader is referred to the web version of this article.)

The spatial density for smaller craters surrounding the landing site is calculated in the 50 m × 50 m grid with the search radius of 100 m and the results for craters larger than 9 m in diameter are shown in Fig. 8c. Generally, the crater distribution in this scale is relatively uniform except that craters on the northern border are a little sparse. It can be attributed to the existence of several very large craters and this also accounts for other low-density areas.

4. Discussion

4.1. Uncertainties in the measurements

The uncertainties of crater diameter and depth are determined by both measurement precision and data quality. The error in identifying the rim points from NAC DOM mosaic (σ_N) can be considered as half a pixel, namely $\sigma_N=\pm 0.45$ m. As described in Jia et al. (2019) and Yue et al. (2019), the measurement uncertainty of crater fitting with three rim points is uncorrelated with the circle diameter but is instead correlated to the distribution of the three selected points. When the three rim points evenly distributed and according to the error propagation law, the produced uncertainty for the fitted radius is $1.16\sigma_N = \pm 0.52$ m (Jia et al., 2019; Yue et al., 2019) for craters measured from NAC mosaic.

The depth measurement uncertainty depends on the DEM height accuracy (Liu et al., 2018). The SLDEM2015 has the typical height accuracy (σ_h) of 3–4 m (Barker et al., 2016) and the NAC DEM used in this study has the height precision of ~1.1 m (Robinson, 2019). Accordingly, the depth uncertainty ($\sigma_d = \sqrt{2}\sigma_h$) is ± 5.7 m for SLDEM and ± 1.6 m for NAC DEM (Liu et al., 2018).

The uncertainty for craters digitalized from PanCam images is influenced by the line of sight direction and distance to the rover. According to the photogrammetric error propagation law (Wang, 1990; Peng et al., 2014), the overall rim point calculation uncertainties (σ_p) are estimated which are no more than ± 0.04 m, ± 0.36 m and ± 0.99 m for craters less than 10 m (48.2% of the catalogue), 30 m (95.1%) and 50 m (99.5%) to the rover, respectively. For diameter calculated by the distance of two ground points, the propagating uncertainties can be approximately $\sqrt{2}\sigma_p$ (Liu et al., 2018), namely ± 0.06 m, ± 0.51 m and ± 1.40 m, respectively.

The depth uncertainty for craters digitalized from PanCam images is similar to that measured from SLDEM or NAC DEM. The topographic influence on depth measurement has been eliminated similar as that in Liu et al. (2018). Due to the closer ranges of the craters for depth measurement, the uncertainties also are smaller and for the smallest crater with a depth of 0.028 and distance of 3.4 m, the depth uncertainty is ± 0.006 m.

4.2. Crater randomness analysis of the multi-scale crater catalogues

The randomness analysis function in CraterStats2 tools is utilized to analyze the crater distribution characteristics. Craters larger than 100 m in the landing area are divided into 9 bins by diameters and the clustering analysis result is displayed in Fig. 9. It can be observed that craters in most ranges tend to be clustered.

For the first and second diameter ranges, i.e., 88 m–120 m (Fig. 9a) and 120 m–180 m (Fig. 9b), the M2CND test rejects randomness with 100% confidence, indicating that craters within these two scales are clustered. In both scales, the denser and sparser areas are substantially consistent with these in the spatial density map (Fig. 8). The incomplete statistic of craters between 88 m–120 m may also be partially accounted for the cluster result. Craters within the diameter range of 120 m–180 m with the amount of 1238 are denser in the eastern part of the landing area, corresponding to the high-density area between 178.0°E and 178.5°E in Fig. 8a, and are likely secondary crater chains. In the next crater bin with the diameter range of 180 m–250 m (Fig. 9c), the M2CND is 1.17 km and it is towards the clustered end of the simulated histogram with a low confidence level of 1.78% to accept the randomness distribution assumption. The crater concentration in the low-right corner of the region mainly accounts for the non-randomness result and it is also applicable for the following two bins. In the crater bin of 500 m–710 m (Fig. 9f), it has a relatively high chance (28.9%) of not rejecting randomness even though the craters in the low-right seem still denser than other areas. The larger crater bins, e.g., the bins from 710 m-1.4 km (Fig. 9g-h), also tend to reject the randomness assumption. The distribution estimation method for the last bin (Fig. 9i) is mean closest neighbour distance since only two craters are involved. The above analysis also demonstrates that the crater chain in the southeast corner
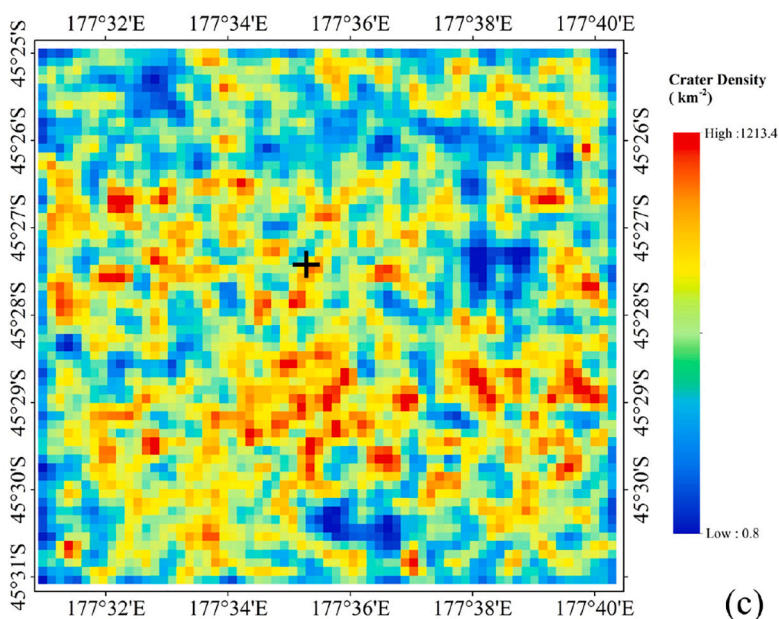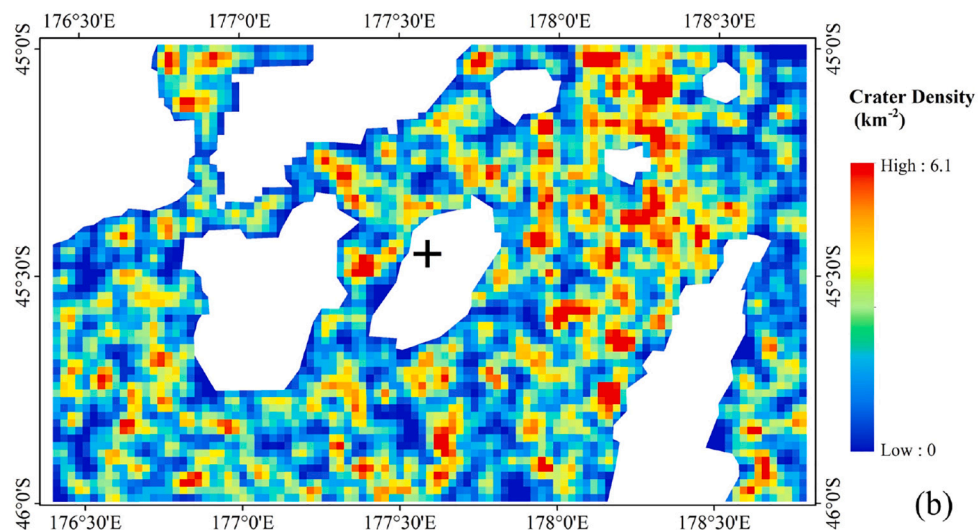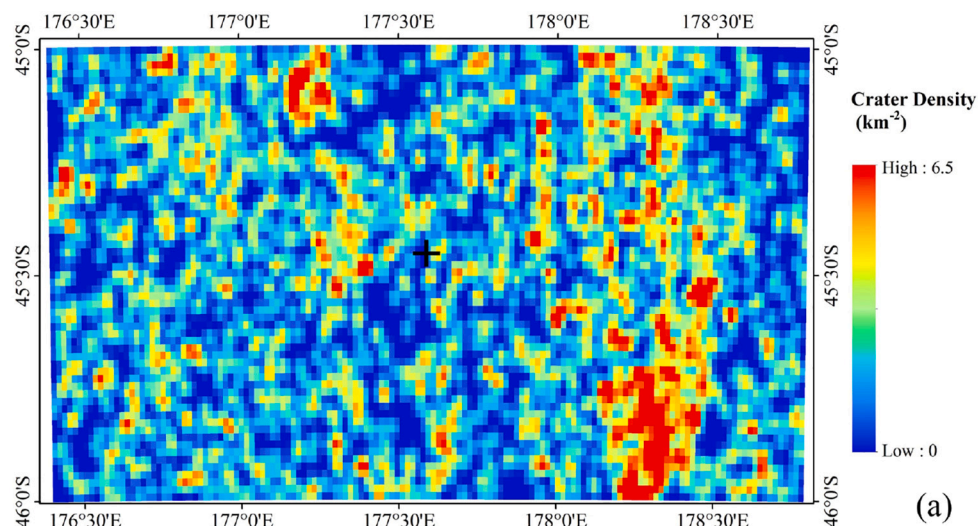
Fig. 8. (a) The spatial density map of all craters larger than 127 m; (b) The spatial density map of craters larger than 127 m excluding possibly secondaries in the landing area. The white areas in (b) indicate the removed secondary chains or clusters. (c) The spatial density map of craters larger than 9 m in diameter in a local 3.2 km × 3.0 km area surrounding the landing site. The CE-4 landing site is marked by black crosses. The search radii (1 km for (a), (b) and 100 m for (c)) are set to make the density maps more smoothly and more visually friendly. Consequently, some craters have been counted more than one time and it is not recommended to deduce the crater number directly from the density maps.
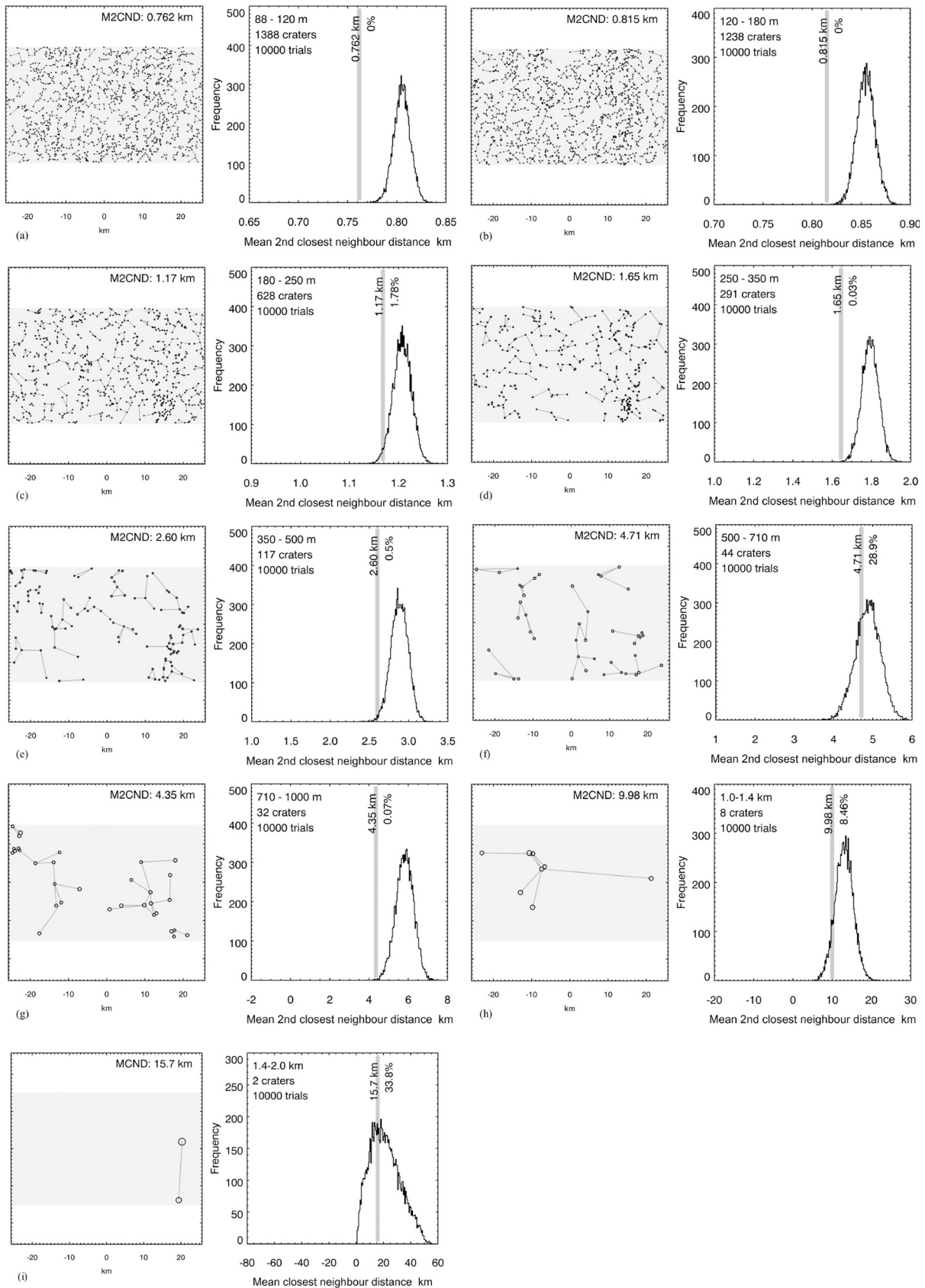
Fig. 9. Randomness analysis of craters larger than ~100 m in diameter (divided into nine groups by diameter) in the landing area. The left plot of each group shows the crater distribution in this diameter range and the right plot compares the M2CND of the measurement with that of the simulated results. The lines connecting craters in the left plots of each group show the 2nd closest neighbour for each crater (Michael et al., 2012).

contains secondaries in very large size ranges (~180 m–700 m), together with their diversely degradation condition from NAC DOM mosaic, likely indicating that they are not formed at the same time period.

The cluster condition of small-sized craters in the local area surrounding the landing site is also investigated in the same way (Fig. 10) and there are 13 crater groups involved. The first two bins are below completeness diameter and they are ignored. Within the diameter range of 7.8 m–11 m (Fig. 10c), the crater population covers almost the whole area and it tends to be randomly distributed by visual interpretation except some areas influenced by the large craters. The M2CND is at the cluster end of the simulated histogram and the low confidence level (1.98%) of accepting the randomness is likely caused by the areas including large craters and several small-scale crater clusters. The next crater bin (11 m–16 m, Fig. 10d) gives a M2CND of 59.4 m, which is larger than the simulated median distance and indicates that craters in this diameter range appear consistent with a random population. Holes still exist due to the presence of large craters. The following two groups (16 m–31 m, Fig. 10e-f) have analogical crater distributions and confidence levels, demonstrating that the populations are consistent with the randomness simulation. For craters within the diameter interval of 31 m–44 m (Fig. 10g), the degree of confidence is relatively low compared with the adjacent bins but still within the simulated histogram. The following four M2CND values (Fig. 10h-k) are nearly centered within the simulated histograms, suggesting the approximately random crater distribution. The last two bins (Fig. 10l-m) are ignored for their limited crater numbers.

By comparing Fig. 9 and Fig. 10, it can be deduced that the large-sized craters (> 100 m in diameter) in the landing area are more clustered than smaller craters in the local 3.2 km × 3.0 km area surrounding the landing site. One of the dominating reasons is that numerous secondary craters larger than 100 m are distributed in the large-scale landing area. There has always been controversial about whether and what scales of small craters on lunar surface is dominant by secondaries. The uniform distribution of small craters in the area surrounding the CE-4 landing site seems to indicate that most of these small craters are primaries and as the continuous observation of CE-4 rover, more evidence may be discovered to verify such deduction.

For the PanCam images are obtained with the optical sight line approximately parallel to the lunar surface, craters could not be measured completely by the occlusion in undulated topography. So craters derived from PanCam images are not involved in randomness
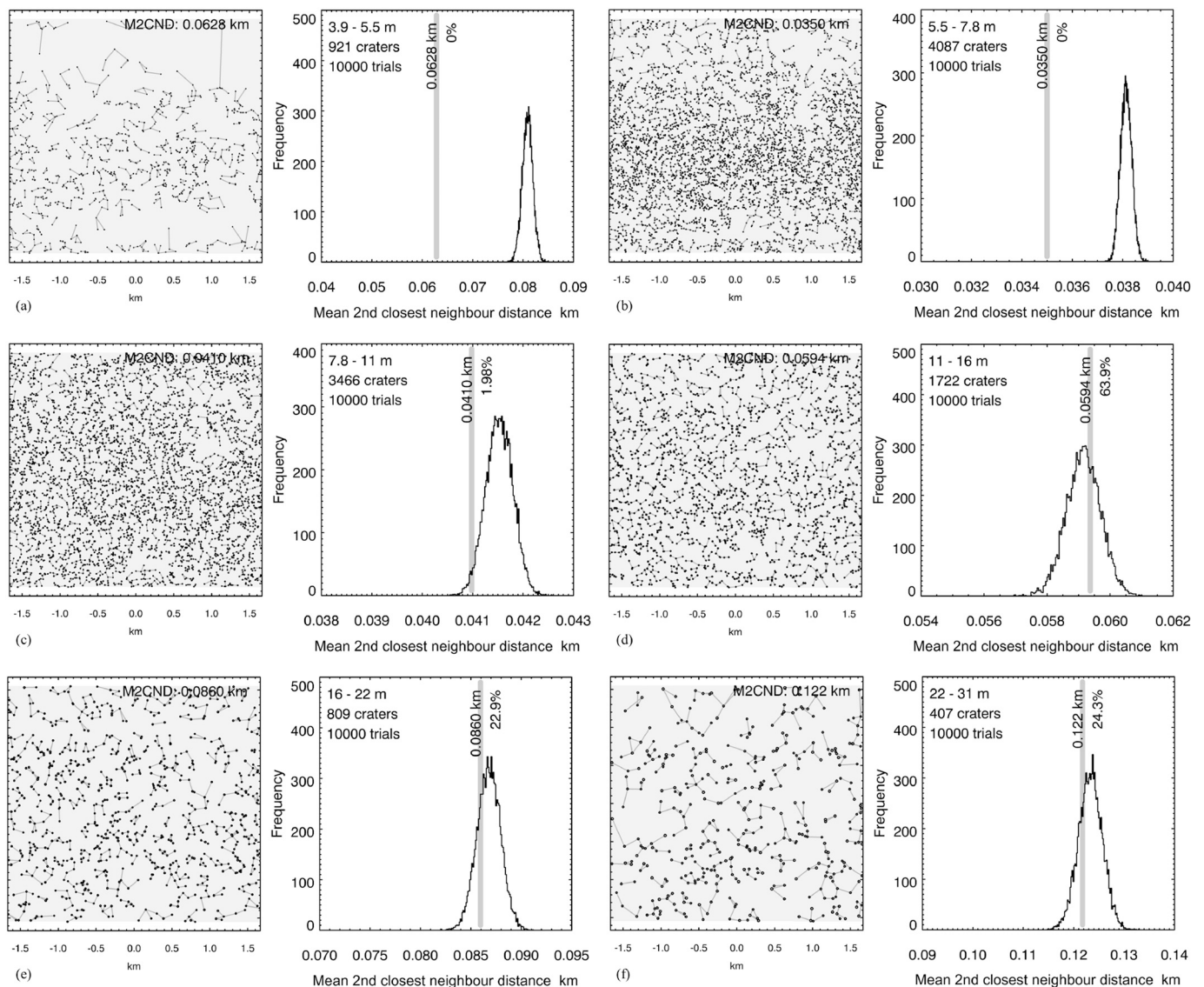

Fig. 10. Randomness analysis of small-sized craters within the 3.2 km × 3.0 km area around the CE-4 landing site. Craters are separated into 13 groups and the configuration of each group is same as that of Fig. 9.
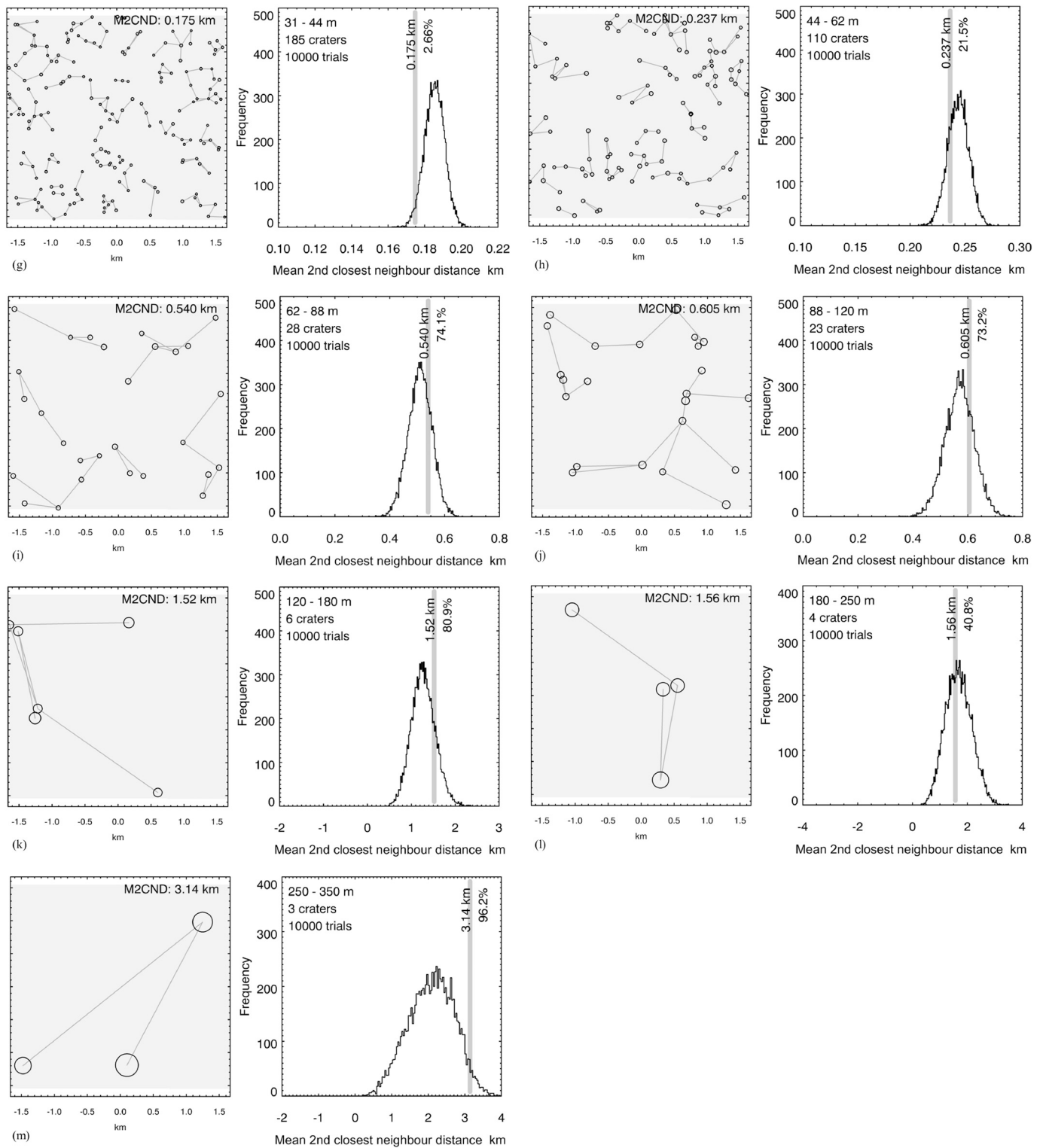
Fig. 10. (*continued*).

analysis and size-frequency distribution analysis.

4.3. Crater size-frequency distribution in the landing area

Crater size-frequency distribution analysis is a powerful tool for studies of planetary surface age (Neukum et al., 1975; Neukum, 1983), bombardment rate (Ivanov, 2006; Ivanov, 2008), surface modification processes (Michael and Neukum, 2010), etc. Thus, even indicated in

Section 4.2 that craters larger than 100 m tend to be clustered in many diameter ranges, we attempted to remove obvious secondary craters by visual interpretation (e.g., Shoemaker et al., 1962; Oberbeck and Morrison, 1973) and to investigate the SFDs of other craters measured from NAC images in two-scales. The removed secondary-crater-related area, which takes ~1/3 of the whole landing area, can be inferred from Fig. 8b.

The CraterStats2 tool (Michael and Neukum, 2010; http://www.geo.

fu-berlin.de/) is used to analyze the SFD in differential (Fig. 11a) and relative (Fig. 11b) modes, respectively. The relative SFD (short as R-plot hereafter) is advantageous in revealing subtle changes (Crater Analysis Techniques Working Group, 1979; Robbins et al., 2018) and the differential plot (D-plot) is useful for identifying possible partial resurfacing events (Michael and Neukum, 2010). The production function (PF) and chronology function (CF) adopted are from Neukum (1983).

For craters obtained from the 3.2 km × 3.0 km area around the landing site (black squares in Fig. 11), it can be discerned from the D-plot that craters smaller than ~90 m deviate from the aging curves. It has been demonstrated that the craters smaller than the equilibrium diameters have lower density than their normal production crater populations (Gault, 1970; Richardson, 2009; Xiao and Werner, 2015). The equilibrium diameter is a demarcation, smaller than which the formation of new craters is balanced by obliteration of old craters due to degradation. Thus, this deviation of crater distribution slope can be attributed to the saturation equilibrium.

The equilibrium phenomenon can also be judged from the R-plot. Several empirical equilibrium levels are included in Fig. 11b with the orange solid line from Hartmann (1984). The other three light-blue dashed horizontal lines are 1%, 5% and 10% of the geometric saturation (N_{gs}), respectively, which was pointed out by Gault (1970) that crater population reaches equilibrium within 1–10% of the geometric saturation level. The cumulative SFD can be expressed as $N = aD^b$, where b indicates the log-log slope of cumulative SFD and the power law index of R-plot is less than the cumulative slope by 1 (Crater Analysis Techniques Working Group, 1979). Another extensively used criterion for crater population equilibrium judgment is the cumulative log-log slope of ~2 (Gault, 1970; Hartmann, 1984; Xiao and Werner, 2015). It can be inferred that all craters in the 3.2 km × 3.0 km area seem to have a cumulative slope of ~2 except some fluctuation between ~90 m and 260 m. The method of Hartmann (1984) gives similar estimation result. Consequently, it can be concluded that craters smaller than 90 m in the 3.2 km × 3.0 km area have reached saturation equilibrium.

For craters larger than 100 m (red stars in Fig. 11), a slope of ~2 can be interpreted for craters smaller than ~250 m from R-plot, and a slight crater distribution density decline can also be observed from Fig. 11a,

indicating that craters smaller than 250 m seems in saturation equilibrium. The law of Hartmann (1984) fails to give equilibrium judgment due to craters in this area having holistic low crater distribution density.

Even though the apparent secondary craters and related areas have been removed, it is still hard to determine the model age from the differential SFD distribution of residual craters. One of the reasons is likely to be the remaining of inconspicuous secondary craters, as described in Qiao et al. (2019) that secondaries are pervasive in the whole landing area. The inconformity formation age of craters can also cause the scattered SFD, which means that a part of craters within the landing area may be formed superposed on the ejecta of other craters, mainly from Finsen crater (Huang et al., 2018; Qiao et al., 2019). Three isochrons are displayed in Fig. 11 (1.3 Ga, 3.2 Ga, 3.6 Ga) and some craters bins between ~250 m and 800 m tend to be closed to the ~1.3 Ga isochron. Age of Finsen crater has been considered as Copernican (Qiao et al., 2019), Eratosthenian, (Wilhelms et al., 1979; Pasckert et al., 2018), or late Imbrium (Ivanov et al., 2018). Thus, the interpretation of craters lying near the ~1.3 Ga isochron partially relies on further careful determination of the age of Finsen crater or other nearby craters whose ejecta covers the CE-4 landing area.

4.4. Depth/diameter ratios of the multi-scale crater catalogues

Continuous observation of lunar surface with high-resolution orbital images and the implementation of lunar landing missions provides the opportunity for the investigation of d/D of very small craters, e.g. in meter scale or even smaller. In this study, the characteristics of d/D in multi-scales, from sub-meter level to kilometer level, are compared and discussed.

From Fig. 6, the distribution of d/D against diameter for all three-scale craters is very scattered especially for those craters with the depth larger than 480 m. Besides, compared with the other two groups, even though more than a half of craters have d/D lower than 0.05, the group with depth obtained from SLDEM2015 contains ten largest d/D (>0.12) in the whole research area, indicating very scattering d/D distribution and the variety of degradation states of the craters. The d/D for craters measured from NAC DEM and PanCam images has similar
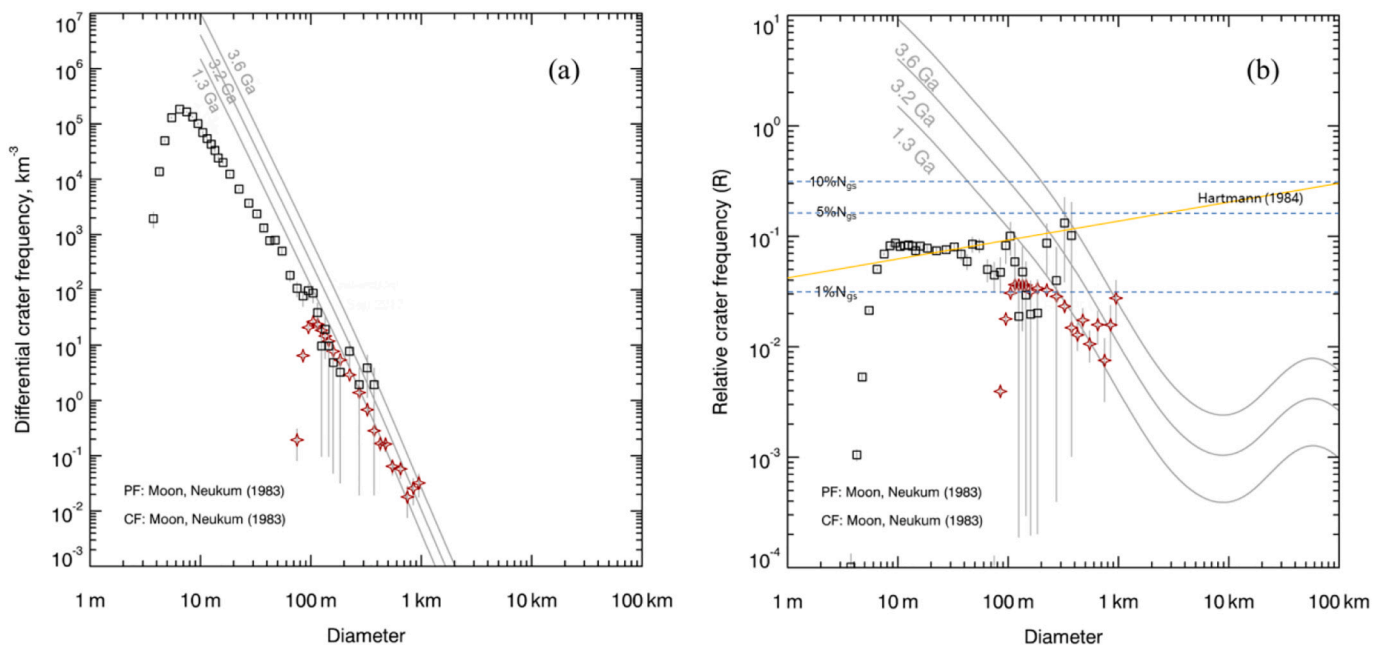

Fig. 11. The size-frequency distributions of craters in differential (a) and relative (b) modes in the CE-4 landing area. Four equilibrium lines (10%, 5%, 1% of the geometric saturation (N_{gs}) and criterion from Hartmann (1984)) are included in the R-plot. Three isochrons (1.3 Ga, 3.2 Ga, 3.6 Ga) are also displayed in two plots. The craters within the 3.2 km × 3.0 km area around the landing site are represented by black squares and larger craters from the whole landing area are shown with red stars. (For interpretation of the references to colour in this figure legend, the reader is referred to the web version of this article.)

distribution range, except those from NAC DEM having a few smaller d/D. One of the reasons for the low d/D values of craters measured from PanCam images is that only those craters close to CE-4 rover or shallow craters in a distance can be measured.

The largest three d/D measured from SLDEM ($D > 480$ m) are 0.18, 0.16 and 0.15, respectively, which have relatively clear rim border but their ejecta blanket is almost indistinguishable. According to historical degradation state grouping criteria, they can be catalogued as B-class craters (Basilevsky et al., 2014; Stopar et al., 2017), and these d/D are roughly consistent with that of Stopar et al. (2017), e.g. 0.192 ± 0.005 for B-class craters with diameter between 400 m–10 km. It is short of fresher large craters, namely A or AB-classes craters, in CE-4 landing area.

For smaller craters measured from NAC DEM ($D < 400$ m), the d/D is obviously smaller than that of larger craters from SLDEM from Fig. 6. The observation in this study is in accord with other exsiting researches focused on d/D of small craters (e.g., Basilevsky et al., 2014; Daubar et al., 2014; Mahanti et al., 2014; Stopar et al., 2017; Sun et al., 2018), that vast majority smaller craters possess d/D lower than that of larger craters (Pike, 1977; Stopar et al., 2017). Besides, there are very limited fresh craters within the 3.2 km × 3.0 km area with only one crater possessing bright ejecta and reliable depth measurement, which can be found from Fig. 1c marked by white arrow and has the d/D of 0.11 (C1 in Table 1). To avoid this low d/D and lack of fresh crater is caused by the limited study area, several small fresh craters with obvious bright ejecta blanket and clear rim border were found from NAC image m1303640934 within the landing area, whose parameters are listed in Table 1. Their d/D values are varied from 0.11 to 0.18 with the mean of 0.14 ± 0.02. The maximum d/D (0.18) is similar to that of larger craters measured from SLDEM, while the larger craters have larger d/D than the craters measured here as a whole.

The reasons for lower d/D for smaller craters can mainly be attributed to that smaller craters essentially have lower d/D values or smaller craters tend to degrade more easily (Fassett and Thomson, 2014), given that they are formed contemporarily with the larger ones. Previous studies (e.g., Melosh, 1989; Stopar et al., 2017) pointed out that the formation of smaller craters are strength-dominated versus gravity-dominated for larger craters. In Sun et al. (2018), it was thought that the difference of strength properties of the surface and shallow subsurface causes the d/D inconsistency of smaller and larger crater. Though craters in all possible degradation levels and even more smaller craters (sub-meter in diameter) are included in this research, the conclusion resembles that craters larger than 480 m on the whole contains larger d/D than the other two group craters. From this point of view, it can be deduced that the d/D of craters seems to increase from sub-meter craters until to those craters on the order of 1 km in diameter since the variation of target property. On the other hand, with similar diameter and apparent morphology, small fresh craters listing in Table 1 have very scattered d/D and it is likely to indicate that smaller craters tend to be more likely to degrade or to be influenced by the target properties, even if their bright ejecta keeps not to be eroded.

Compared with existing results (e.g., Basilevsky et al., 2014; Mahanti et al., 2015; Stopar et al., 2017; Sun et al., 2018), the most distinct feature of d/D in CE-4 landing area is the scarcity of craters with large d/D (>0.18), no matter for crater measures from SLDEM or NAC DEM. This can be partially ascribed to old geologic age of the area. In addition, the subsequent post-Von Kármán impacting events, e.g., Alder and Finsen cratering, may also enhance the degradation of craters, causing the scarcity of large fresh craters in the research area.

5. Conclusion

This research mapped three crater catalogues with different scales in the CE-4 landing area, and the spatial distribution characteristics and morphological properties are analyzed. The analysis focuses on three scales: craters larger than 100 m covering the whole landing area

Table 1

Information about some relatively fresh craters surrounding the CE-4 landing site. The C1 crater can be seen from Fig. 1c pointed by a white arrow.

Crater ID	Longitude (°)	Latitude (°)	Diameter (m)	Depth (m)	d/D
C1	177.626	−45.420	59.7	6.3	0.11
C2	177.584	−45.866	113.19	20.33	0.18
C3	177.347	−45.868	147.16	22.44	0.15
C4	177.670	−45.526	118.66	17.70	0.15
C5	177.735	−45.499	116.17	17.24	0.15
C6	177.486	−45.777	107.26	15.37	0.14
C7	177.517	−45.619	92.33	12.51	0.14
C8	177.625	−45.744	170.89	21.92	0.13
C9	177.572	−45.903	126.86	16.15	0.13
C10	177.576	−45.577	103.96	12.88	0.12
C11	177.619	−45.569	63.60	7.13	0.11

(176.4°E-178.8°E, 45°S-46°S), all craters in local scale (3.2 km × 3.0 km) surrounding the landing site, and craters surrounding the rover measured from one station of the Yutu-2 PanCam images. Completeness analysis demonstrates that the first crater catalogue completed in ~127 m and the second one has a complete diameter of ~9 m.

The spatial density investigation of the catalogue with crater larger than 127 m indicates that distinct secondary craters cover at least 1/3 of the landing area and mainly influence the eastern part of the landing area except several scattered secondary clusters in the west. The spatial density for small-scaled craters within the 3.2 km × 3.0 km area is relatively uniform. The randomness analysis reveals more elaborate crater spatial distribution and results show that craters larger than 100 m are almost in non-random distribution in all the size ranges.

The size-frequency distribution reveals that craters smaller than 90 m within 3.2 km × 3.0 km area and smaller than 250 m of the whole landing area tend to reach saturation equilibrium. The comparison of d/D of the three-scale crater catalogues indicates that larger craters have relatively larger d/D. The surface and subsurface material difference may partially account for this phenomenon. One-hundred-meter-scale fresh craters with bright ejecta and clear rim border have varied d/D values, indicating that small craters seem to be more easily to degrade or or to be influenced by the target properties, even their bright ejecta keeps uneroded. The scarcity of craters with large d/D (>0.18) in the research areas can be partially ascribed to old geologic age of the area as well as the subsequent post-Von Kármán impacting events. Further effort, like physical impact experiment or numerical simulation can devote to uncover the mechanism of the observation.

Declaration of Competing Interest

None

Appendix A. Supplementary data

Supplementary data to this article can be found online at https://doi.org/10.1016/j.icarus.2020.114164.

References

Neukum, G., 1983. Meteoritenbombardement und Datierung planetarer Oberflächen, Habilitationsschrift (habilitation thesis), Univ. München, Munich, Germany. Meteorite bombardment and dating of planetary surfaces (English translation, 1984). Habilitation Thesis for Faculty Membership. University of Munich, p. 186.

Anderson, J.A., Sides, S.C., Soltesz, D.L., et al., 2014. Modernization of the integrated software for imagers and spectrometers. In: Lunar and planetary science conference. Abstract #2039.

Barker, M.K., Mazarico, E., Neumann, G.A., et al., 2016. A new lunar digital elevation model from the lunar orbiter laser altimeter and SELENE terrain camera. Icarus 273, 346–355.

Basilevsky, A.T., Kreslavsky, M.A., Karachevtseva, I.P., et al., 2014. Morphometry of small impact craters in the Lunokhod-1 and Lunokhod-2 study areas. Planet. Space Sci. 92, 77–87.

Bland, M.T., Raymond, C.A., Schenk, P.M., et al., 2016. Composition and structure of the shallow subsurface of Ceres revealed by crater morphology. Nat. Geosci. 9 (7), 538.

CLEP, 2018. The data release of CE-2 Global digital orthophoto model (7m) [2019-4-15]. http://moon.bao.ac.cn/pubMsg/detail-dom7EN.jsp.

Crater Analysis Techniques Working Group, 1979. Standard techniques for presentation and analysis of crater size-frequency data. Icarus 37, 467–474. https://doi.org/10.1016/0019-1035(79)90009-5.

Daubar, I.J., Atwood-Stone, C., Byrne, S., McEwen, A.S., Russell, P.S., 2014. The morphology of small fresh craters on Mars and the Moon. J. Geophys. Res. 119 (12), 2620–2639. https://doi.org/10.1002/2014JE0 04671.

Di, K., Liu, Z., Liu, B., et al., 2019a. Chang'e-4 lander localization based on multi-source data. J. Remote Sensing 23 (1), 177–184.

Di, K., Zhu, M., Yue, Z., et al., 2019b. Topographic evolution of Von Kármán crater revealed by the lunar rover Yutu-2. Geophys. Res. Lett. 46, 12764–12770.

Fassett, C.I., Thomson, B.J., 2014. Crater degradation on the lunar maria: topographic diffusion and the rate of erosion on the Moon. J. Geophys. Res. 119 (10), 2255–2271.

Gao, Y., Ge, Y., Ma, L., et al., 2019. Optimization design of configuration and layout for Queqiao relay satellite. Adv. Astronaut. Sci. Technol. 1–6.

Gault, D.E., 1970. Saturation and equilibrium conditions for impact cratering on the lunar surface: criteria and implications. Radio Sci. 5, 273–291.

Gou, S., Di, K., Yue, Z., et al., 2019. Lunar deep materials observed by Chang'e-4 rover. Earth Planet. Sci. Lett. 528 (115829), 1–9.

Gou, S., Yue, Z., Di, K., et al., 2020. In situ spectral measurements of space weathering by Chang'e-4 rover. Earth Planet. Sci. Lett. 535, 116–117.

Hartmann, W.K., 1984. Does crater "saturation equilibrium" occur in the solar system? Icarus 60 (1), 56–74.

Head, J.W., Murchie, S., Mustard, J.F., et al., 1993. Lunar impact basins: new data for the western limb and far side (Orientale and south pole-Aitken basins) from the first Galileo flyby. J. Geophys. Res. 98 (E9), 17149–17181.

Henriksen, M.R., Manheim, M.R., Burns, K.N., et al., 2017. Extracting accurate and precise topography from LROC narrow angle camera stereo observations. Icarus 283, 122–137.

Hu, X., Ma, P., Yang, Y., et al., 2019. Mineral abundances inferred from in situ reflectance measurements of Chang'E-4 landing site in South Pole-Aitken Basin. Geophys. Res. Lett. 46 (16), 9439–9447.

Huang, J., Xiao, Z., Flahaut, J., et al., 2018. Geological characteristics of Von Kármán crater, northwestern south pole-Aitken Basin: Chang'E-4 landing site region. J. Geophys. Res. 123 (7), 1684–1700.

Ivanov, B.A., 2006. Earth/Moon impact rate comparison: searching constraints for lunar secondary/primary cratering proportion. Icarus 183 (2), 504–507.

Ivanov, B.A., 2008. Size-Frequency Distribution of Asteroids and Impact Craters: Estimates of Impact Rate. Catastrophic events caused by cosmic objects. Springer, Dordrecht, pp. 91–116.

Ivanov, M.A., Hiesinger, H., van der Bogert, C.H., et al., 2018. Geologic history of the northern portion of the South Pole-Aitken basin on the Moon. J. Geophys. Res. 123 (10), 2585–2612.

Jia, Y., Zou, Y., Ping, J., et al., 2018. The scientific objectives and payloads of Chang'E-4 mission. Planet. Space Sci> 162, 207–215.

Jia, M., Yue, Z., Di, K., et al., 2019. A reanalysis of the relationship between the size of boulders and craters in lunar surface. Icarus 331, 116–126.

Kneissl, T., Van Gasselt, S., Neukum, G., 2011. Map–projection–independent crater size-frequency determination in GIS environments–new software tool for ArcGIS. Planet. Space Sci. 59, 1243–1254.

Li, C., Liu, D., Liu, B., et al., 2019. Chang'E-4 initial spectroscopic identification of lunar far-side mantle-derived materials. Nature 569, 378–382.

Liu, Z., Yue, Z., Michael, G., Gou, S., Di, K., Sun, S., Liu, J., 2018. A global database and statistical analyses of (4) Vesta craters. Icarus 311, 242–257.

Liu, B., Niu, S., Xin, X., et al., 2019. High precision DTM and DOM generating using multi-source orbital data on Chang'e-4 landing site. In: ISPRS Geospatial Week 2019-GSW2019, "International workshop on Planetary Remote Sensing and Mapping", 10–14 June, Enschede, The Netherlands, pp. 1413–1417.

Lucey, P.G., Taylor, G.J., Hawke, B.R., Spudis, P.D., 1998. FeO and TiO$_2$ concentrations in the South Pole-Aitken basin: implications for mantle composition and basin formation. J. Geophys. Res. 103 (E2), 3701–3708.

Mahanti, P., Robinson, M.S., Stelling, R., 2014. How deep and steep are small lunar craters? New insights from LROC NAC DEMs. In: 45th Lunar and Planetary Science Conference. Abstract #1584.

Mahanti, P., Robinson, M.S., Stelling, R., 2015. How old are small lunar craters? A depth-to-diameter ratio based Analyis. In: 46th lunar and planetary science conference. Abstract #1615.

Melosh, H.J., 1989. Impact cratering: A geologic process. Oxford University Press, New York, p. 253.

Melosh, H.J., Kendall, J., Horgan, B., Johnson, B.C., Bowling, T., Lucey, P.G., Taylor, G. J., 2017. South Pole–Aitken basin ejecta reveal the Moon's upper mantle. Geology 45 (12), 1063–1066.

Michael, G.G., Neukum, G., 2010. Planetary surface dating from crater size–frequency distribution measurements: partial resurfacing events and statistical age uncertainty. Earth Planet. Sci. Lett. 294, 223–229.

Michael, G.G., Platz, T., Kneissl, T., et al., 2012. Planetary surface dating from crater size–frequency distribution measurements: spatial randomness and clustering. Icarus 218 (1), 169–177.

Neukum, G., Koenig, B., Arkani-Hamed, J., 1975. A study of lunar impact crater size-distributions. Moon 12 (2), 201–229.

Oberbeck, V.R., Morrison, R.H., 1973. On the formation of the lunar herringbone pattern. In: 4th Lunar Planetary Science Conference, 4, pp. 107–123.

Ohtake, M., Uemoto, K., Yokota, Y., et al., 2014. Geologic structure generated by large-impact basin formation observed at the South Pole-Aitken basin on the Moon. Geophys. Res. Lett. 41 (8), 2738–2745.

Pasckert, J.H., Hiesinger, H., van der Bogert, C.H., 2018. Lunar farside volcanism in and around the South Pole–Aitken basin. Icarus 299, 538–562.

Peng, M., Wan, W., Wu, K., et al., 2014. Topographic mapping capability analysis of Chang'e-3 Navcam stereo images and three-dimensional terrain reconstruction for mission operations. J. Remote Sensing 18, 995–1002.

Pike, R.J., 1977. Apparent depth/apparent diameter relation for lunar craters. In: 8th Lunar and planetary science conference, pp. 3427–3436.

Povilaitis, R.Z., Robinson, M.S., van der Bogert, C.H., Hiesinger, H., Meyer, H.M., Ostrach, L.R., 2018. Crater density differences: exploring regional resurfacing, secondary crater populations, and crater saturation equilibrium on the moon. Planet. Space Sci. 162, 41–51.

Qiao, L., Ling, Z., Fu, X., et al., 2019. Geological characterization of the Chang'e-4 landing area on the lunar farside. Icarus 333, 37–51.

Qin, S.H., Huang, Y., Li, P.J., et al., 2019. Orbit and tracking data evaluation of Chang'E-4 relay satellite. Adv. Space Res. 64, 836–846.

Richardson, J.E., 2009. Cratering saturation and equilibrium: a new model looks at an old problem. Icarus 204, 697–715.

Robbins, S.J., 2019. A new global database of lunar impact craters >1–2 km: 1. Crater locations and sizes, comparisons with published databases, and global analysis. J. Geophys. Res. 124.

Robbins, S.J., Riggs, J.D., Weaver, B.P., et al., 2018. Revised recommended methods for analyzing crater size-frequency distributions. Meteorit. Planet. Sci. 53, 891–931.

Robinson, M., 2019. Topographic map of the Chang'e-4 Site [2019-4-30]. http://lroc.sese.asu.edu/posts/1100.

Robinson, M.S., Brylow, S.M., Tschimmel, M., et al., 2010. Lunar reconnaissance orbiter camera (LROC) instrument overview. Space Sci. Rev. 150, 81–124.

Shoemaker, E.M., Hackman, R.J., Eggleton, R.E., 1962. Interplanetary correlation of geologic time. Adv. Astronaut. Sci. 8, 70–79.

Soderblom, L.A., Condit, C.D., West, R.A., et al., 1974. Martian planetwide crater distributions: implications for geologic history and surface processes. Icarus 22 (3), 239–263.

Stopar, J.D., Robinson, M.S., Barnouin, O., et al., 2017. Relative depths of simple craters and the nature of the lunar regolith. Icarus 298, 34–48.

Sun, S., Yue, Z., Di, K., 2018. Investigation of the depth and diameter relations of subkilometer-diameter lunar craters. Icarus 309, 61–68.

Wang, Z.Z., 1990. Principles of Photogrammetry (With Remote Sensing). Press of Wuhan Technical University of Surveying and Mapping and Publishing House of Surveying and Mapping, Beijing, pp. 327–330.

Wilhelms, D.E., Howard, K.A., Wilshire, H.G., Kozak, R., 1979. Geologic map of the south side of the moon. IMAP 1162.

Wilhelms, D.E., McCauley, J.F., Trask, N.J., 1987. The geologic history of the Moon. USGS Professional Paper 1348. US Government Printing Office, Washington DC, pp. 1–281.

Wood, C.A., Anderson, L., 1978. New morphometric data for fresh lunar craters. In: Lunar and planetary science conference proceedings, pp. 3669–3689.

Wu, W., Li, C., Zuo, W., et al., 2019. Lunar farside to be explored by Chang'e-4. Nat. Geosci. 12 (4), 222–223.

Xiao, Z., Werner, S.C., 2015. Size-frequency distribution of crater populations in equilibrium on the Moon. J. Geophys. Res. Planets 120 (12), 2277–2292.

Yue, Z., Di, K., Liu, Z., et al., 2019. Lunar regolith thickness deduced from concentric craters in the CE-5 landing area. Icarus 329, 46–54.

Zhao, B.C., Yang, J.F., Wen, D.S., et al., 2011. Overall scheme and on-orbit images of Chang'E-2 lunar satellite CCD stereo camera. SCIENCE CHINA Technol. Sci. 54 (9), 2237.